

Coupling of Erbium-Implanted Silicon to a Superconducting Resonator

Mark A. Hughes,^{1,*} Naitik A. Panjwani,^{2,3} Matias Urdampilleta,^{2,4} Nafsika Theodoropoulou,¹ Ilana Wisby,^{5,6,7} Kevin P. Homewood,^{8,9} Ben Murdin,⁸ Tobias Lindström,⁵ and J. David Carey^{8,10}

¹*Materials and Physics Research Group, School of Science, Engineering and Environment, University of Salford, Salford M5 4WT, United Kingdom*

²*London Centre for Nanotechnology, University College London, Gower Place, WC1E 6BT London, United Kingdom*

³*Berlin Joint EPR Lab, Fachbereich Physik, Freie Universität Berlin, 14195 Berlin, Germany*

⁴*Institut Néel-CNRS-UJF-INPG, UPR2940 25 rue des Martyrs BP 166, 38042 Grenoble Cedex 9, France*

⁵*National Physical Laboratory, Hampton Road, Teddington TW11 0LW, United Kingdom*


⁶*Royal Holloway, University of London, Egham TW20 0EX, United Kingdom*

⁷*Oxford Quantum Circuits Ltd., King Charles House 2nd Floor, Park End Street, Oxford, Oxfordshire OX1 1JD, United Kingdom*

⁸*Advanced Technology Institute, Faculty of Engineering and Physical Sciences, University of Surrey, Guildford GU2 7XH, United Kingdom*

⁹*School of Materials Science and Engineering, Hubei University, Wuhan 430062, People's Republic of China*

¹⁰*Department of Electrical and Electronic Engineering, University of Surrey, Guildford GU2 7XH, United Kingdom*

 (Received 11 February 2021; revised 13 May 2021; accepted 16 August 2021; published 2 September 2021)

Erbium-implanted silicon is promising for both photonic and quantum-technology platforms, since it possesses both telecommunications and integrated-circuit processing compatibility. However, several different Er centers are generated during the implantation and annealing process, the presence of which could hinder the development of these applications. When Si is coimplanted with 10^{17} cm^{-3} Er and 10^{20} cm^{-3} O ions, and the appropriate annealing process is used, one of these centers, which is present at higher Er concentrations, can be eliminated. Characterization of samples with Er concentrations of $<10^{17} \text{ cm}^{-3}$ is limited by the sensitivity of standard electron paramagnetic resonance (EPR) instruments. The collective coupling strength between a superconducting (SC) NbN lumped-element resonator and a 10^{17} cm^{-3} Er-implanted Si sample at 20 mK is measured to be about 1 MHz, which provides a basis for the characterization of low-concentration Er-implanted Si and for future networks of hybrid quantum systems that exchange quantum information over the telecommunication network. Of six known Er-related EPR centers, only one trigonal center couples to the SC resonator.

DOI: [10.1103/PhysRevApplied.16.034006](https://doi.org/10.1103/PhysRevApplied.16.034006)

I. INTRODUCTION

When Er is coimplanted with O into Si, a variety of EPR- and photoluminescence (PL) active centers can be observed. The PL-active centers are proposed as a platform for developing all-silicon photonic technology solutions that would eliminate the undesirable need for discrete direct-band-gap semiconductor devices to interface with the fiber-optic telecommunications network [1]. The EPR-active centers are proposed as a platform for developing quantum technologies (QTs), since using Er-implanted Si links the decoupling from the environment of the partially filled $4f$ shell inherent to all rare earths

with the integrated-circuit fabrication pedigree of silicon [2,3]. We have recently reported an electron-spin coherence time from Er-implanted Si, with an Er concentration of $3 \times 10^{17} \text{ cm}^{-3}$, of $7.5 \mu\text{s}$ at 5 K [4], which compares to $1.6 \mu\text{s}$ at 1.9 K for about $2 \times 10^{18} \text{ cm}^{-3}$ Er:Y₂SiO₅ [5] and about $5 \mu\text{s}$ at 5 K for about 10^{16} cm^{-3} Er:CaWO₄ [6]. This is promising given the difficulty in repairing defects after implantation that could lead to decoherence. To date, one of the main issues in the development of the photonic and quantum-technology applications of Er-implanted Si has been the difficulty in characterizing, identifying, and controlling the large number of EPR- and PL-active centers that are generated; a solution to this problem is offered through coupling the Er spin ensemble to a superconducting (SC) resonator, which can provide

*m.a.hughes@salford.ac.uk

sensitivity enhancements over traditional EPR techniques. For example, by exploiting SC-resonator coupling, the EPR signal from Er:Y₂SiO₅ can be detected with about 1 fW of microwave power [7], and the sensitivity for Bi spins in Si is 65 spins/ $\sqrt{\text{Hz}}$ [8].

As well as offering advantages for the EPR characterization of a spin ensemble, the coupling of a SC resonator to a spin ensemble can itself constitute a hybrid quantum system with many advantages for quantum-information processing over either individual system. If the interactions of a superconducting resonator coupled to a spin ensemble are mediated with one or a few superconducting qubits, a system possessing both the long coherence times of the spin ensemble and the fast gating of the superconducting qubits can be formed, in which case the hybrid quantum system can behave as a quantum Turing machine with the spin ensemble forming a microwave quantum memory and the SC qubits performing the gate operations [9,10]. The use of rare earths as a spin ensemble is beneficial because they generally possess large g factors, as the orbital angular momentum is not quenched, which is advantageous for strong coupling [11], and long coherence times, which is advantageous for quantum memory [2]. The successful storage and on-demand retrieval of 16 weak coherent microwave pulses from Er:Y₂SiO₅ has been demonstrated [12], and a single ensemble could be used to store many qubits by using holographic encoding [13]. In addition, ensembles of rare-earth ions coupled to SC resonators are proposed for microwave-to-optical transducers for quantum networks [11,14]. The coherent conversion of single-microwave to telecoms-wavelength photons would allow applications such as optical-fiber links between separate quantum processors and the deterministic entanglement of telecoms-wavelength photons [15]. We have previously demonstrated that under 1.5- μm illumination an EPR resonance from a PL-active Er center with orthorhombic symmetry in Er-implanted Si can be observed, which has an intensity 3 orders of magnitude higher than that of unilluminated EPR resonances [2]. This shows that the microwave and optical transitions required for various proposed microwave-to-optical transducer schemes involving rare earths [16,17] are present in a single Er center in Er-implanted Si. Other features that make Er-implanted Si attractive for quantum-information processing include the demonstration of deterministic single-ion implantation of rare-earth ions with a placement precision of 34 nm [18].

Optical and magnetic characterization of Er-implanted Si presents a significant challenge in detecting a PL or EPR signal because of the relatively low number of Er centers compared with those in the bulk, the low implant yield for any particular center (the yield for all optically active Er centers varies between 1% and 10% for different studies [1]), and the indirect band gap of silicon. As such, EPR and PL characterization is typically carried out with a high Er concentration, typically 10^{19} cm^{-3} [1,19].

Here, we report EPR and PL results from a sample with as low as 10^{17} cm^{-3} Er and coupling between Er-implanted in Si and a superconducting resonator, which could have applications in further characterization and identification of the centers of Er-implanted Si, to enable quantum and photonic technology applications, and in the development microwave quantum memory and microwave-to-optical transducers.

II. EXPERIMENT

Two samples, with Er concentrations of 10^{17} and 10^{19} cm^{-3} , both with O concentrations of 10^{20} cm^{-3} , are prepared by implanting Er and O ions into $\langle 100 \rangle$ -oriented (8000 ± 500) Ωcm Si wafer. Samples are then annealed at 620 °C for 180 min to recrystallize the amorphized region and then at 850 °C for 30 s to activate Er; it was previously found that annealing at 850 °C significantly increased the EPR-signal strength [2]. For all samples, O and Er ions are implanted at a range of energies to give a flat concentration profile down to a depth of around 1.5 μm , see Fig. S1 within the Supplemental Material [20]. Isotope-specific implantation is used, so that only zero-nuclear-spin ¹⁶⁶Er is implanted.

EPR measurements are performed on a Bruker E580 EPR spectrometer, with the magnetic field, B_0 , parallel to the [001] direction of the wafer with an uncertainty of $\pm 5^\circ$. All EPR measurements are made at 10 K, with a microwave frequency of 9.61 GHz, and a modulation width of 2 G. The microwave power used is 0.5 and 2.5 mW for the 10^{17} cm^{-3} Er and 10^{19} cm^{-3} Er samples, respectively. PL spectra are obtained by cooling the sample in a cold-finger LN₂ cryostat at 65 K. Excitation is by a 462-nm 10-mW laser diode, and the generated fluorescence is dispersed in a Bentham TMc300 monochromator, with a resolution of 1 nm, and detected with an IR photomultiplier tube coupled with standard phase-sensitive detection.

SC-resonator coupling measurements are performed in a dilution refrigerator, fitted with a vector magnet, at 20 mK. A superconducting lumped-element microresonator is fabricated by sputtering 200 nm of NbN, patterned by standard e -beam lithography, onto an R -cut sapphire substrate. The 10^{17} cm^{-3} Er sample is “flip-chipped” on top of the microresonator and pressed down using Cu-Be springs. The microresonator is placed in a magnetic field that is stepped from 0 to 930 G. The power in the resonator is about 3 pW. At each magnetic field, the microwave transmission coefficient, S_{21} , is measured using a vector network analyzer. This is repeated for magnetic field orientations between 0° and 160° in steps of 5°, with 0° corresponding to B_0 parallel to the face of the resonator and sample. The magnetic field is rotated around the [110] crystal axis of the sample. Numerical fitting of the S_{21} response of the

microresonator is used to extract the total measured loss tangent, $\tan\delta_{\text{tot}}=1/Q_{\text{tot}}$, where Q_{tot} is the total measured Q factor and $\tan\delta_{\text{tot}}=\tan\delta_c+\tan\delta_{\text{diel}}+\tan\delta_B+\tan\delta_{\text{ions}}$ are the loss tangents due to coupling to the transmission line, dielectric losses, the external magnetic field, and the Er ions, respectively. Numerical fitting is used to extract $\tan\delta_{\text{ions}}$. A discussion of the loss mechanisms is given in the Supplemental Material [20].

III. RESULTS AND DISCUSSION

A. EPR measurements

When implanted into Si, Er exists in its usual 3+ oxidation state [1]. Oxygen is coimplanted to a concentration of 10^{20} cm^{-3} for both samples and is required to generate narrow Er-related EPR [21] and PL [22] lines by the creation of various O-coordinated Er centers. PL lines from a Si-coordinated Er center with cubic symmetry, Er-C, can be observed without O coimplantation [22]. PL lines from an O-coordinated Er center with orthorhombic C_{2v} symmetry and an unidentified O-coordinated Er center, referred to as Er-O1R and PL- U , respectively, are reported [2]. Previous measurements of the angular dependence of the Er-related EPR lines in Er-implanted Si identify a number of different O-coordinated Er EPR centers: three monoclinic C_{1h} centers labeled OEr-1, OEr-1', and OEr-3 and three trigonal C_{3v} centers labeled OEr-2, OEr-2', and OEr-4 [19,21,23,24]. An unidentified EPR center, EPR- U , with resonances at about 1700 G, using the same B_0 orientation as us, has been reported [21]. Zeeman measurements of molecular-beam-epitaxy- (MBE) grown Er-doped Si identify an orthorhombic O-coordinated Er center [25], which is not EPR active, and we argue is the same center as that of Er-O1R we have previously identified [2]. A summary of all these centers, including their g factors, is given in Table I. The isotropic g factor for the cubic center is calculated from crystal-field analysis of the PL measurements [26].

Figure 1 shows the EPR spectra of the 10^{17} cm^{-3} Er and 10^{19} cm^{-3} Er samples. By comparison with the angular dependencies of the previously reported EPR centers in Table I, we can assign a unique center to all of the observed resonances. Notably, a small angular deviation in the $[1\bar{1}0]$ axis can cause significant shifting of the EPR resonances. The most intense resonances for both the 10^{17} cm^{-3} Er and 10^{19} cm^{-3} Er samples at about 925 G, attributed to the OEr-1 and OEr-3 monoclinic centers, all have widths of about 5 G, whereas the resonances for both samples at about 2200 G, attributed to the OEr-2' trigonal centers, all have widths of about 20 G. The independence of linewidth over such a large concentration range indicates that clustering does not affect the spin linewidth, and therefore, both centers are homogeneously distributed. In Er:Y₂SiO₅, there are two Er centers with different g factors: when coupled to a SC resonator, it is found that the spin linewidth of the

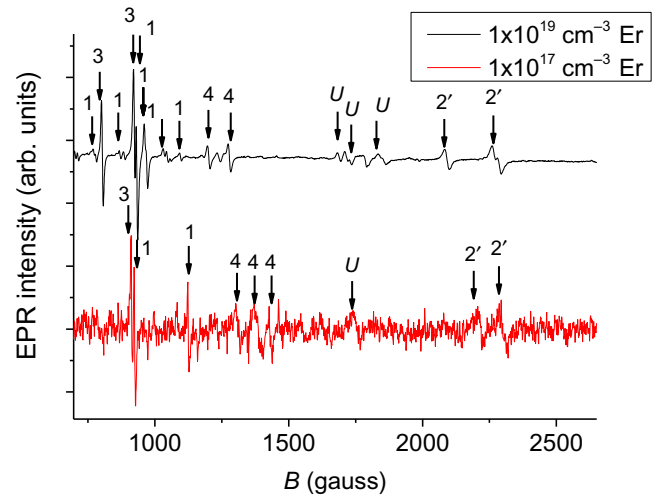


FIG. 1. EPR spectra of 10^{17} cm^{-3} Er and 10^{19} cm^{-3} Er-implanted Si. Resonances are assigned to the EPR centers in Table I, OEr-1, OEr-2' etc., as 1,2' etc., and U is the unidentified EPR center. Microwave frequency is 9.61 GHz, and magnetic field is parallel to the $[001]$ direction of the wafer.

center with a smaller g factor is greater than the center with a large g factor; this is attributed to inhomogeneities in the dc magnetic field [27]. However, transitions with a larger g factor are more susceptible to inhomogeneities in the magnetic field, which also broadens the inhomogeneous spin linewidth. The balance of these effects depends on alignment [27], which could explain the difference in EPR linewidth between the monoclinic and trigonal Er centers that we observe.

B. Photoluminescence measurements

Figure 2 shows the PL spectra of the 10^{17} cm^{-3} Er and 10^{19} cm^{-3} Er samples. In the 10^{19} cm^{-3} Er spectrum, we can identify peaks from the Er-C, the Er-O1R orthorhombic center, and PL- U unidentified centers [2], as indicated. The most intense peak at about 6510 cm^{-1} can be attributed to both the Er-C and Er-O1R centers [2]. In the 10^{17} cm^{-3} Er spectrum, no peaks unique to the Er-C center can be identified, indicating that the Er-C center is not present in the 10^{17} cm^{-3} Er sample. This indicates that the 1000:1 O:Er ratio in the 10^{17} cm^{-3} Er sample is effective at eliminating the Er-C Si-coordinated center because of the relative abundance of O. Additional peaks at 6450 and 6495 cm^{-1} not observed in the 10^{19} cm^{-3} Er spectrum can be identified; it cannot be determined at this stage if these originate from the same unidentified center, which gives peaks at $>6510\text{ cm}^{-1}$.

The PL linewidths are broadly similar for the 10^{17} cm^{-3} Er and 10^{19} cm^{-3} Er spectra: about 20 cm^{-1} for the identifiable peaks. There are some small but significant shifts in the peak positions attributed to the orthorhombic center of the 10^{17} cm^{-3} Er spectrum compared with the

TABLE I. Summary of the known EPR- and PL-active centers in Er-implanted Si.

Center	Symmetry	Local coordination	g_x	g_y	g_z	Ref.
EPR-active centers						
OEr-1	Monoclinic C_{1h}	O	0.8	5.45	12.6	[21]
OEr-1'	Monoclinic C_{1h}	O	0.8	5.45	12.55	[21]
OEr-3	Monoclinic C_{1h}	O	1.09	5.05	12.78	[21]
OEr-4	Trigonal C_{3v}	O	2.0	6.23	6.23	[21]
OEr-2	Trigonal C_{3v}	O	0.45	3.46	3.22	[21]
OEr-2'	Trigonal C_{3v}	O	0.69	3.24	3.24	[21]
EPR- U	—	O	—	—	—	[21]
PL-active centers						
Er-O1R	Orthorhombic C_{2v}	O	~ 0	~ 0	18.4	[2,25]
Er-C	Cubic T_d	Si	6.8	—	—	[2,21,26]
PL- U	—	O	—	—	—	[2]

10^{19} cm^{-3} Er spectrum, particularly the main peak at about 6510 cm^{-1} and the highest-energy orthorhombic peak at about 6570 cm^{-1} , which could represent a subtle change in the structure of this center.

Crystal-field analysis of rare-earth spectra can be used to find crystal-field parameters (CFP), which measure the interaction between the f -shell electrons of rare earths and their surrounding crystalline environment. Each possible symmetry of the rare earth's environment has its own set of CFPs. The Hamiltonian (H) of a rare earth in a magnetic field can be described as

$$H = H_F + H_{CF} + H_{Ze}. \quad (1)$$

H_F accounts for the interactions that occur in a free rare-earth ion and is responsible for the energy of the J manifolds. Each rare earth has its own set of H_F parameters, which vary slightly between crystal hosts; those given by Carnall *et al.* for Er:LaF₃ are used here [28]. H_{CF}

represents the perturbation generated by the ligand field surrounding a rare-earth ion. The multipole expansion of H_{CF} is the linear combination of a set of spherical tensors, $C_q^{(k)}$, and a corresponding set of structural factors, B_q^k , which are the crystal-field parameters:

$$H_{CF} = \sum_{k,q} B_q^k C_q^{(k)}. \quad (2)$$

A description of the $C_q^{(k)}$ spherical-tensor-operator matrix can be found elsewhere [3]. Diagonalizing H_{CF} gives the crystal-field energy levels of the J manifold. To find the CFPs, we fit CFPs that minimize the sum of squares difference between the calculated and experimental energy levels using the Levenberg-Marquardt algorithm. The Zeeman interaction, H_{Ze} , is given by

$$H_{Ze} = g_J \mu_B \mathbf{J} \cdot \mathbf{H}, \quad (3)$$

where g_J is the Landé factor, μ_B is the Bohr magneton, \mathbf{J} is the angular momentum operator, and \mathbf{H} is the magnetic field strength [29]. H_{Ze} is not considered during the fitting procedure. Once the Er³⁺ CFPs are determined, the g tensor for any crystal-field doublet can be calculated from their eigenvectors, $|+\rangle$ and $|-\rangle$. The diagonal components of the g tensor, g_x , g_y , and g_z , can then be calculated from the first-order perturbation expressions [29]:

$$\begin{aligned} g_x &= 2g_J \langle + | \mathbf{J}_x | - \rangle, \\ g_y &= 2g_J \langle + | \mathbf{J}_y | - \rangle, \\ g_z &= 2g_J \langle + | \mathbf{J}_z | + \rangle, \end{aligned} \quad (4)$$

where \mathbf{J}_x , \mathbf{J}_y , and \mathbf{J}_z are the vector components of \mathbf{J} , such that $\mathbf{J}^2 = \mathbf{J}_x^2 + \mathbf{J}_y^2 + \mathbf{J}_z^2$.

We fit the orthorhombic C_{2v} set of CFPs to the Er-O1R center PL lines in Fig. 2; the PL lines at $< 6200 \text{ cm}^{-1}$ cannot be resolved in the 10^{17} cm^{-3} Er spectrum, so we use those from the 10^{19} cm^{-3} Er spectrum. We also use the

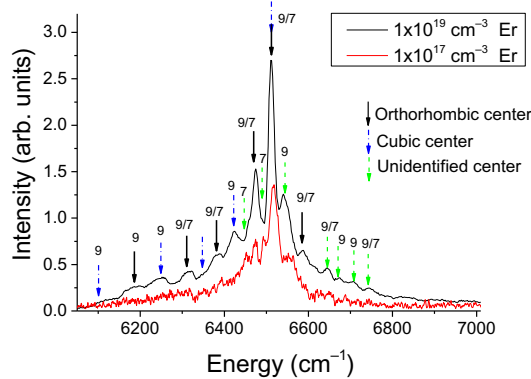


FIG. 2. PL spectra of 10^{17} cm^{-3} Er and 10^{19} cm^{-3} Er-implanted Si at 65 K. PL peaks are assigned to orthorhombic Er-O1R, cubic Er-C, and unknown (PL- U) PL centers in Table I with arrows. Arrows are marked with 9, 7, or 9/7 if the peaks can be identified in the 10^{19} cm^{-3} Er spectrum, 10^{17} cm^{-3} Er spectrum, or both spectra, respectively.

TABLE II. Fitted orthorhombic C_{2v} crystal-field parameters for 10^{19} cm^{-3} Er and 10^{17} cm^{-3} Er PL.

Er conc. (cm^{-3})	C_{2v} crystal-field parameters (cm^{-1})								
	B_0^2	B_0^4	B_0^6	B_2^2	B_2^4	B_4^4	B_2^6	B_4^6	B_6^6
10^{19}	-72 ± 3	-2085 ± 36	3 ± 7	159 ± 6	-208 ± 21	262 ± 11	-260 ± 7	-109 ± 4	-30 ± 10
10^{17}	-58 ± 10	-1879 ± 49	18 ± 8	569 ± 59	-258 ± 38	214 ± 24	-284 ± 29	40 ± 31	4 ± 26

hot line previously identified for this center [22] to give the required number of crystal-field levels to fit the nine orthorhombic C_{2v} CFPs, which are given in Table II.

To interpret the CFPs, recognizing how the orthorhombic set of CFPs arises from progressive distortions of higher-symmetry groups can be helpful. Cubic symmetry is described by four CFPs with constraints: $B_4^4 = 5B_0^4$ and $B_4^6 = -21B_0^6$ [30]. With a tetragonal distortion to a cubic field, the B_0^2 parameter appears, so it belongs only to the tetragonal component of the crystal field [31] and is therefore dependent on the degree of axial asymmetry. An orthorhombic distortion to a purely tetragonal field is described by addition of the B_2^2 , B_2^4 , B_2^6 , and B_6^6 parameters.

The calculated CFPs for the 10^{19} cm^{-3} Er spectrum are almost identical to what we have previously determined for 10^{19} cm^{-3} Er [2]; however, there are some important differences in the 10^{17} cm^{-3} Er CFPs. B_0^2 is smaller, indicating there is less tetragonal distortion, whereas the magnitude of the four CFPs representing an orthorhombic distortion are all greater, except for B_6^6 , indicating a greater degree of orthorhombic distortion. Using the eigenvectors from our CFP fitting and Eq. (4), we calculate g factors for 10^{17} and 10^{19} cm^{-3} Er as $g_x \approx 0$, $g_y \approx 0$, $g_z = 17.6$ and $g_x \approx 0$, $g_y \approx 0$, $g_z = 17.9$, respectively, showing that any change in the structure of the Er-O1R at 10^{17} cm^{-3} Er has an insignificant effect on the g factor.

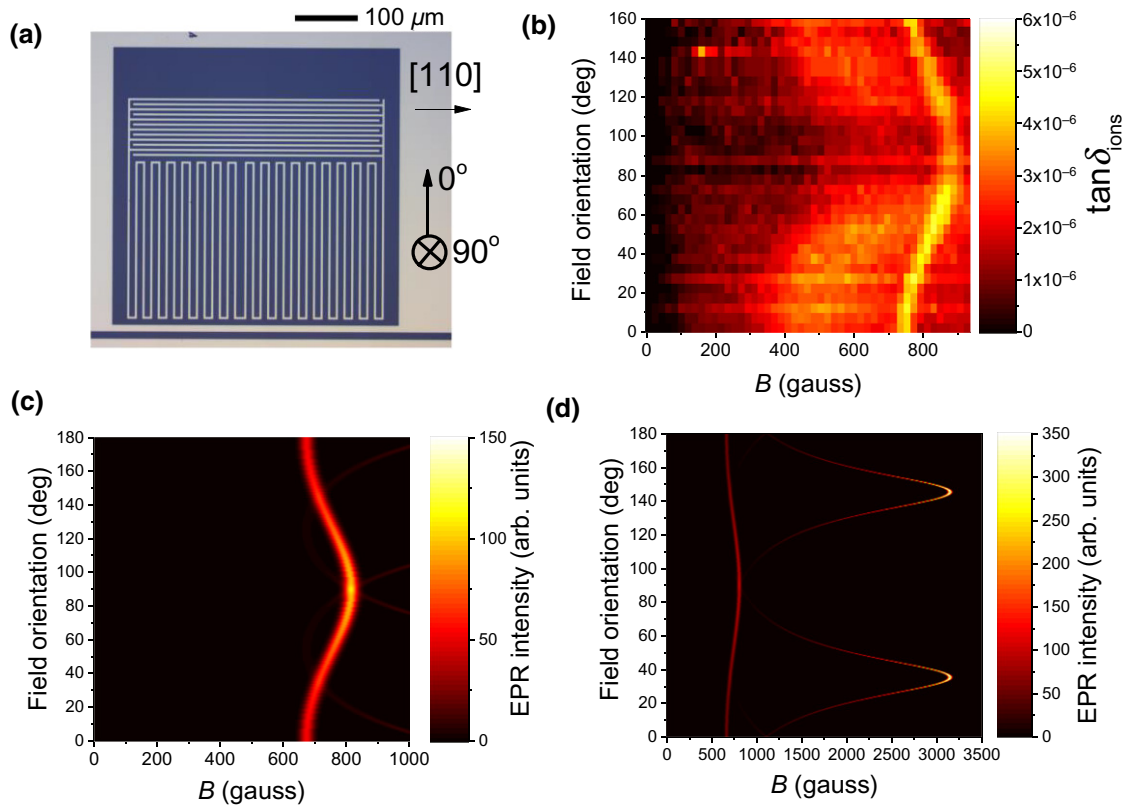


FIG. 3. (a) Image of the SC resonator that is coupled to the 10^{17} cm^{-3} Er sample. The [110] direction of the sample, which is placed on top of and covers the resonator, is shown, along with the 0° and 90° directions of the magnetic field. (b) Angular-dependent microresonator EPR measurements at 20 mK. (c) Simulated angular-dependent EPR spectrum using EASYS PIN numerical modeling for the trigonal OEr-2' center identified by Carey *et al.* [21] with $g_{CA} = 0.69$ and $g^\perp = 3.24$. (d) Simulated angular-dependent EPR extended to higher B_0 to show the positions of the three expected EPR resonances with trigonal symmetry. Microwave frequency is 3.04 GHz for all microresonator measurements and simulations.

C. Superconducting-resonator coupling

The implanted face of the 10^{17} Er cm $^{-3}$ sample is placed in contact with the superconducting NbN lumped-element microresonator on *R*-cut Al $_2$ O $_3$, shown in Fig. 3(a), which has a center frequency of $\omega_r/2\pi = 3.04$ GHz, see Sec. II. Figure 3(b) shows the loss tangents due to coupling to Er ions ($\tan\delta_{\text{ions}}$) as a function of B_0 and orientation. There is a single narrow resonance, with a FWHM of (50 ± 10) G, that varies smoothly between 740 and 870 G, depending on the B_0 orientation. There is also a very broad resonance centered at 500 G and at B_0 parallel to [001] (0° orientation); the resonance shifts to 600 G at 50° B_0 orientation. We simulate the angular dependence of the six EPR centers (three trigonal, three monoclinic) previously identified Er- and O-implanted Si system [21], see Table I, but find no correspondence with this broad resonance. The narrow resonance corresponds to the trigonal OEr-2' center identified in Ref. [21] with $g_{\parallel} = 0.69$ and $g^{\perp} = 3.24$, which is shown in the simulation in Fig. 3(c). The two other resonances are also visible in this B_0 range but are significantly weaker, which explains why only one resonance is observed in the microresonator measurement. A higher B_0 range shows the positions of all three expected EPR resonances with trigonal symmetry in the simulation in Fig. 3(d). Only one previously identified OEr-2' trigonal center is evident in the microresonator measurements at 20 mK; however, standard EPR measurements of the 10^{17} Er cm $^{-3}$ at 10 K show the presence of the OEr-1 monoclinic center. This indicates that the spin-lattice relaxation time, T_1 , of the OEr-1 center is long enough at 20 mK to cause saturation of the coupling signal, but not for the OEr-2' center.

The Q factor of a resonator coupled to an ensemble of spins can be modeled as a single-mode harmonic oscillator according to

$$Q_{\text{tot}} = \frac{\Delta^2 + \gamma^2}{2g_{\text{col}}^2\gamma + \kappa(\Delta^2 + \gamma^2)}\omega_r, \quad (5)$$

where Δ is the detuning from the spin-resonance peak; γ is the spin linewidth; κ is the cavity linewidth, which is $2\pi\omega_r/Q_{\text{tot}} = 0.56$ MHz for the 0° orientation and is independently measured away from the resonance for each B_0 orientation; Q_{tot} is the total measured cavity Q ; and g_{col} is the collective coupling strength. Figure 4 shows the fitting of Eq. (5) to Q_{tot} for the 0° orientation, which gives $g_{\text{col}}/2\pi = 1$ MHz and $\gamma/2\pi = 80$ MHz. The average for all B_0 orientations is $g_{\text{col}}/2\pi = (1.1 \pm 0.3)$ MHz and $\gamma/2\pi = (85 \pm 25)$ MHz. The coupling strength of an individual spin to the SC resonator is given by $g_i = g_{\text{col}}/\sqrt{N}$, where N is the number of spins coupled to the resonator; using the number of Er ions above the inductive element (Er dose \times inductive element area = 3.7×10^{10}) gives a lower limit for g_i of about 6 Hz, since the implantation yield is unknown for this EPR center. This compares

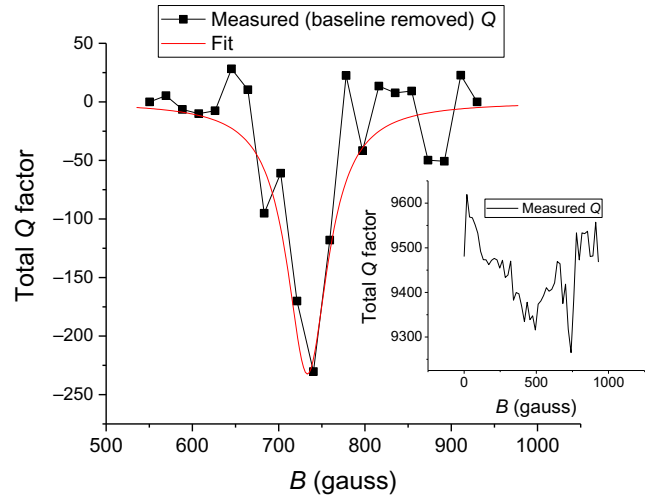


FIG. 4. Measured Q factor, with the baseline subtracted, of the microresonator EPR measurement with a field orientation of 0° fitted using Eq. (5). Inset shows the total measured Q factor without baseline subtraction.

to $g_i \sim 70$ Hz for an Er-implanted Y $_2$ SiO $_5$ crystal [14]. We calculate the expected collective coupling strength, $g_{\text{col,Calc}}$, by numerically simulating, then integrating over, the magnetic field and implanted-ion distributions. Details of this simulation are given in the Supplemental Material [20], and further details can be found in Refs. [32–36]. Our numerical simulation provides $g_{\text{col,Calc}} \sim 3$ MHz, which is, to a first approximation, consistent with the measured g_{col} and similar to what we have calculated previously for Gd-implanted Al $_2$ O $_3$ coupled to a microresonator [37]. We observe no change in ω_r as B_0 is swept through the Er-spin resonance, indicating the system is operating in the weak-coupling regime. The signal-to-noise ratio (SNR) is calculated from $\text{SNR} = (A_{\text{signal}}/A_{\text{noise}})^2$, where A_{signal} and A_{noise} are the signal and noise amplitudes, respectively. For the microresonator EPR measurement shown in Fig. 4, the SNR is 140 ± 30 ; this compares with a SNR of 5 ± 2 for the EPR spectrum of the same OEr-2' center, with a similar sweep time. Our microresonator measurement demonstrates the coupling of a SC resonator to a rare-earth ensemble implanted in Si and a significant improvement in SNR compared with standard EPR.

IV. CONCLUSIONS

When the Er concentration is reduced from 10^{19} to 10^{17} cm $^{-3}$, but the O concentration is kept at 10^{20} cm $^{-3}$, no change in EPR linewidth is observed, indicating that concentration effects are not important. The Si-coordinated Er center with cubic symmetry is no longer evident in PL measurements. Some small PL peak shifts of the O-coordinated Er center with orthorhombic symmetry are observed at 10^{17} cm $^{-3}$ Er. Crystal-field analysis of these PL peaks indicates that the orthorhombic Er center has less

tetragonal distortion, but greater orthorhombic distortion at 10^{17} cm^{-3} Er. Reducing the Er concentration, while keeping a relatively high O concentration, may be an effective strategy to further reduce the numerous Er centers that are generated; however, detection by standard EPR techniques presents a challenge for characterization at low concentrations; a solution could be to exploit SC-resonator coupling. We observe coupling between a SC resonator and Er-implanted Si with $g_{\text{col}}=1$ MHz and $g_i > 6$ Hz, which provides a basis for characterization of low-concentration Er-implanted Si and for future networks of hybrid quantum processors that exchange quantum information over the telecommunication network. Numerical simulations indicate an expected g_{col} of about 3 MHz. Of six known Er-related EPR centers, only one trigonal center couples to the SC resonator at 20 mK.

Datasets generated during the current study are available in the Mendeley Data repository [38].

ACKNOWLEDGMENTS

This work is supported by the UK EPSRC Grants No. EP/R011885/1 and No. EP/H026622/1. We would like to thank Prof. John Morton for helpful discussions.

The concept was developed by M.A.H. Experimental work was performed by M.A.H., N.A.P., M.U., N.T., and I.W. with input from J.D.C. and T.L. The manuscript was written by M.A.H. with editorial input from J.D.C., K.P.H., and B.M. All authors contributed to analyzing the results and commented on the paper.

-
- [1] A. J. Kenyon, Erbium in silicon, *Semicond. Sci. Technol.* **20**, R65 (2005).
- [2] M. A. Hughes, H. Li, N. Theodoropoulou, and J. D. Carey, Optically modulated magnetic resonance of erbium implanted silicon, *Sci. Rep.* **9**, 19031 (2019).
- [3] M. A. Hughes, M. A. Lourenço, J. D. Carey, B. Murdin, and K. P. Homewood, Crystal field analysis of Dy and Tm implanted silicon for photonic and quantum technologies, *Opt. Express* **22**, 29292 (2014).
- [4] M. A. Hughes, N. A. Panjwani, M. Urdampilleta, K. P. Homewood, B. Murdin, and J. D. Carey, Spin echo from erbium implanted silicon, *Appl. Phys. Lett.* **118**, 194001 (2021).
- [5] S. Welinski, P. J. Woodburn, N. Lauk, R. L. Cone, C. Simon, P. Goldner, and C. W. Thiel, Electron Spin Coherence in Optically Excited States of Rare-Earth Ions for Microwave to Optical Quantum Transducers, *Phys. Rev. Lett.* **122**, 247401 (2019).
- [6] S. Bertaina, S. Gambarelli, A. Tkachuk, I. N. Kurkin, B. Malkin, A. Stepanov, and B. Barbara, Rare-earth solid-state qubits, *Nat. Nanotechnol.* **2**, 39 (2007).
- [7] P. Bushev, A. Feofanov, H. Rotzinger, I. Protopopov, J. Cole, C. Wilson, G. Fischer, A. Lukashenko, and A. Ustinov, Ultralow-power spectroscopy of a rare-earth spin ensemble using a superconducting resonator, *Phys. Rev. B* **84**, 060501 (2011).
- [8] S. Probst, A. Bienfait, P. Campagne-Ibarcq, J. Pla, B. Albanese, J. Da Silva Barbosa, T. Schenkel, D. Vion, D. Esteve, and K. Mølmer, Inductive-detection electron-spin resonance spectroscopy with 65 spins/Hz sensitivity, *Appl. Phys. Lett.* **111**, 202604 (2017).
- [9] Y. Kubo, F. Ong, P. Bertet, D. Vion, V. Jacques, D. Zheng, A. Dréau, J.-F. Roch, A. Auffèves, and F. Jelezko, Strong Coupling of a Spin Ensemble to a Superconducting Resonator, *Phys. Rev. Lett.* **105**, 140502 (2010).
- [10] B. Julsgaard, C. Grezes, P. Bertet, and K. Mølmer, Quantum Memory for Microwave Photons in an Inhomogeneously Broadened Spin Ensemble, *Phys. Rev. Lett.* **110**, 250503 (2013).
- [11] G. Dold, C. W. Zollitsch, J. O'sullivan, S. Welinski, A. Ferrier, P. Goldner, S. de Graaf, T. Lindström, and J. J. Morton, High-Cooperativity Coupling of a Rare-Earth Spin Ensemble to a Superconducting Resonator Using Yttrium Orthosilicate as a Substrate, *Phys. Rev. Appl.* **11**, 054082 (2019).
- [12] S. Probst, H. Rotzinger, A. V. Ustinov, and P. A. Bushev, Microwave multimode memory with an erbium spin ensemble, *Phys. Rev. B* **92**, 014421 (2015).
- [13] J. H. Wesenberg, K. Mølmer, L. Rippe, and S. Kröll, Scalable designs for quantum computing with rare-earth-ion-doped crystals, *Phys. Rev. A* **75**, 012304 (2007).
- [14] S. Probst, N. Kukharchyk, H. Rotzinger, A. Tkalčec, S. Wünsch, A. D. Wieck, M. Siegel, A. V. Ustinov, and P. A. Bushev, Hybrid quantum circuit with implanted erbium ions, *Appl. Phys. Lett.* **105**, 162404 (2014).
- [15] J. J. Morton and P. Bertet, Storing quantum information in spins and high-sensitivity ESR, *J. Magn. Reson.* **287**, 128 (2018).
- [16] L. A. Williamson, Y.-H. Chen, and J. J. Longdell, Magneto-Optic Modulator with Unit Quantum Efficiency, *Phys. Rev. Lett.* **113**, 203601 (2014).
- [17] X. Fernandez-Gonzalvo, Y.-H. Chen, C. Yin, S. Rogge, and J. J. Longdell, Coherent frequency up-conversion of microwaves to the optical telecommunications band in an Er : YSO crystal, *Phys. Rev. A* **92**, 062313 (2015).
- [18] K. Groot-Berning, T. Kornher, G. Jacob, F. Stopp, S. T. Dawkins, R. Kolesov, J. Wrachtrup, K. Singer, and F. Schmidt-Kaler, Deterministic Single-Ion Implantation of Rare-Earth Ions for Nanometer-Resolution Color-Center Generation, *Phys. Rev. Lett.* **123**, 106802 (2019).
- [19] J. D. Carey, J. F. Donegan, R. C. Barklie, F. Priolo, G. Franzò, and S. Coffà, Electron paramagnetic resonance of erbium doped silicon, *Appl. Phys. Lett.* **69**, 3854 (1996).
- [20] See the Supplemental Material at <http://link.aps.org/supplemental/10.1103/PhysRevApplied.16.034006> for the simulated implant profile and numerical simulation of collective coupling strength.
- [21] J. D. Carey, R. C. Barklie, J. F. Donegan, F. Priolo, G. Franzò, and S. Coffà, Electron paramagnetic resonance and photoluminescence study of Er-impurity complexes in Si, *Phys. Rev. B* **59**, 2773 (1999).
- [22] H. Przybylinska, W. Jantsch, Y. Suprun-Belevitch, M. Stepikhova, L. Palmetshofer, G. Hendorfer, A. Kozanecki, R. J. Wilson, and B. J. Sealy, Optically active erbium centers in silicon, *Phys. Rev. B* **54**, 2532 (1996).

- [23] J. D. Carey, R. C. Barklie, J. F. Donegan, F. Priolo, G. Franzò, and S. Coffa, EPR study of erbium-impurity complexes in silicon, *J. Lumines.* **80**, 297 (1998).
- [24] J. D. Carey, Structure of multi-oxygen-related defects in erbium-implanted silicon, *J. Phys.-Condes. Matter* **14**, 8537 (2002).
- [25] N. Q. Vinh, H. Przybylińska, Z. F. Krasil'nik, and T. Gregorkiewicz, Microscopic Structure of Er-Related Optically Active Centers in Crystalline Silicon, *Phys. Rev. Lett.* **90**, 066401 (2003).
- [26] S. Laachir, M. Moussetad, and R. Adhiri, Crystal-Field energy levels of trivalent Erbium ion in cubic symmetry, *Zeitschrift für Naturforschung A* **66**, 457 (2011).
- [27] S. Probst, *Hybrid Quantum System Based on Rare Earth Doped Crystals* (Karlsruher Institut für Technologie, Karlsruhe, 2015).
- [28] W. Carnall, G. Goodman, K. Rajnak, and R. Rana, A systematic analysis of the spectra of the lanthanides doped into single crystal LaF₃, *J. Chem. Phys.* **90**, 3443 (1989).
- [29] A. Abragam and B. Bleaney, *Electron Paramagnetic Resonance of Transition Ions* (Oxford University Press, Oxford, 1970).
- [30] K. R. Lea, M. J. M. Leask, and W. P. Wolf, The raising of angular momentum degeneracy of f-electron terms by cubic crystal fields, *J. Phys. Chem. Solids* **23**, 1381 (1962).
- [31] P. Pal, T. Penhouet, V. D'Anna, and H. Hagemann, Effect of pressure on the free ion and crystal field parameters of Sm²⁺ in BaFBr and SrFBr hosts, *J. Lumines.* **134**, 678 (2013).
- [32] I. Wisby, PhD Thesis, Royal Holloway, University of London, 2017.
- [33] J. Burnett, T. Lindström, M. Oxborrow, Y. Harada, Y. Sekine, P. Meeson, and A. Y. Tzalenchuk, Slow noise processes in superconducting resonators, *Phys. Rev. B* **87**, 140501 (2013).
- [34] A. Megrant, C. Neill, R. Barends, B. Chiaro, Y. Chen, L. Feigl, J. Kelly, E. Lucero, M. Mariani, and P. J. O'Malley, Planar superconducting resonators with internal quality factors above one million, *Appl. Phys. Lett.* **100**, 113510 (2012).
- [35] J. Burnett, L. Faoro, I. Wisby, V. Gurtovoi, A. Chernykh, G. Mikhailov, V. Tulin, R. Shaikhaidarov, V. Antonov, and P. Meeson, Evidence for interacting two-level systems from the 1/f noise of a superconducting resonator, *Nat. Commun.* **5**, 1 (2014).
- [36] A. A. B. Brojeny, Y. Mawatari, M. Benkraouda, and J. R. Clem, Magnetic fields and currents for two current-carrying parallel coplanar superconducting strips in a perpendicular magnetic field, *Supercond. Sci. Technol.* **15**, 1454 (2002).
- [37] I. Wisby, S. E. de Graaf, R. Gwilliam, A. Adamy, S. E. Kubatkin, P. J. Meeson, A. Y. Tzalenchuk, and T. Lindström, Coupling of a locally implanted rare-earth ion ensemble to a superconducting micro-resonator, *Appl. Phys. Lett.* **105**, 102601 (2014).
- [38] <http://dx.doi.org/10.17632/stpfvbp8yc.1>